






Article

Segmenting Cervical Arteries in Phase Contrast Magnetic Resonance Imaging Using Convolutional Encoder–Decoder Networks

Britney Campbell ^{1,2,†}, Dhruv Yadav ^{1,3,†}, Ramy Hussein ¹, Maria Jovin ¹ , Sierrah Hoover ¹, Kim Halbert ¹, Dawn Holley ¹, Mehdi Khalighi ¹ , Guido A. Davidzon ¹ , Elizabeth Tong ¹, Gary K. Steinberg ⁴, Michael Moseley ¹, Moss Y. Zhao ^{1,*}  and Greg Zaharchuk ^{1,*} 

¹ Department of Radiology, Stanford University, Stanford, CA 94305, USA

² Department of Chemical Engineering, University of South Florida, Tampa, FL 33620, USA

³ Department of Computer Science, University of Washington, Seattle, WA 98195, USA

⁴ Department of Neurosurgery, Stanford University, Stanford, CA 94305, USA

* Correspondence: mosszhao@stanford.edu (M.Y.Z.); gregz@stanford.edu (G.Z.)

† These authors contributed equally to this work.

‡ These authors share senior authorship.

Abstract: Phase contrast (PC) magnetic resonance imaging (MRI) is a primary method used to quantify blood flow. Cerebral blood flow (CBF) is an important hemodynamic parameter to characterize cerebrovascular and neurological diseases. However, a critical step in CBF quantification using PC MRI is vessel segmentation, which is largely manual, and thus time-consuming and prone to inter-rater variability. Here, we present encoder–decoder deep learning models to automate segmentation of neck arteries to accurately quantify CBF. The PC-MRI data were collected from 46 Moyamoya (MM) patients and 107 healthy control (HC) participants. Three segmentation U-Net models (Standard, Nested, and Attention) were compared. The PC MRI images were taken before and 15 min after vasodilation. The models were assessed based on their ability to detect the internal carotid arteries (ICAs), external carotid arteries (ECAs), and vertebral arteries (VAs), using the Dice score coefficient (DSC) of overlap between manual and predicted segmentations and receiver operator characteristic (ROC) metric. Analysis of variance, Wilcoxon rank-sum test, and paired *t*-test were used for comparisons. The Standard U-NET, Attention U-Net, and Nest U-Net models achieved results of mean DSCs of 0.81 ± 0.21 , and 0.85 ± 0.14 , and 0.85 ± 0.13 , respectively. The ROC curves revealed high area under the curve scores for all methods (≥ 0.95). While the Nested and Attention U-Net architectures accomplished reliable segmentation performance for HC and MM subsets, Standard U-Net did not perform as well in the subset of MM patients. Blood flow velocities calculated by the models were statistically comparable. In conclusion, optimized deep learning architectures can successfully segment neck arteries in PC MRI images and provide precise quantification of their blood flow.

Keywords: deep learning; phase contrast MRI; blood flow; Moyamoya



Citation: Campbell, B.; Yadav, D.; Hussein, R.; Jovin, M.; Hoover, S.; Halbert, K.; Holley, D.; Khalighi, M.; Davidzon, G.A.; Tong, E.; et al. Segmenting Cervical Arteries in Phase Contrast Magnetic Resonance Imaging Using Convolutional Encoder–Decoder Networks. *Appl. Sci.* **2023**, *13*, 11820. <https://doi.org/10.3390/app132111820>

Academic Editors: Donato Cascio and Cosimo Nardi

Received: 12 September 2023

Revised: 12 October 2023

Accepted: 26 October 2023

Published: 29 October 2023



Copyright: © 2023 by the authors. Licensee MDPI, Basel, Switzerland. This article is an open access article distributed under the terms and conditions of the Creative Commons Attribution (CC BY) license (<https://creativecommons.org/licenses/by/4.0/>).

1. Introduction

Sufficient blood supply in the brain is important to maintain a healthy cerebral blood flow (CBF) and cerebral autoregulation [1]. Impaired CBF caused by vasculopathy can affect cerebral autoregulation and increase the risk for cerebrovascular diseases and neurological disorders [2]. Moyamoya disease is a progressive cerebrovascular disorder that disturbs normal CBF; patients with Moyamoya have a higher risk for acute and recurrent strokes [3]. Since the brain receives its blood supply directly from the internal carotid and vertebral arteries, measuring the blood flow within these arteries can directly reflect CBF and autoregulation [4]. Several medical imaging modalities have been developed to measure

blood flow volume in arteries and arterioles. For instance, phase contrast (PC) MRI is an imaging technique that is commonly used to characterize blood flow velocity without the need for radiation and contrast agents [5]. The measured blood flow velocity may lead to the computation of total flow volume. Several studies have demonstrated the effectiveness of PC MRI in measuring blood flow in patients with arteriopathy [6]. However, its clinical application has been limited by the need for manual segmentation of multiple vessels of interest. This not only deteriorates the reproducibility of the measurements using PC MRI, but also affects quantitative measurements of blood flow. Although commercial software is available for the segmentation of PC MRI, the procedures also require adjustment of operators and thus have many of the same problems as the fully manual method.

Deep learning is a class of machine learning that has shown great promise in several medical imaging applications [7]. Among the advanced deep learning techniques, deep convolutional neural networks (CNN) have been applied in segmentation and lesion detection tasks in medical imaging [8]. Using acquired data as the input and desired data as the output, a model is trained to determine the optimal parameters for the transformation between input and output. The difference between the output and ground truth is used to adjust the parameters of the model to improve the prediction iteratively. Once trained (or the parameter values determined), the model can be applied to predict the output associated with a new input. For example, an encoder–decoder framework has been applied in segmenting PC MRI of cardiac images to enable fully automated aortic flow quantification, leading to markedly improved efficiency and reproducibility of the segmentation task [9]. In the realm of applications in cervical cancer, several previous studies demonstrated that deep learning methods were developed to identify cervical cancer to improve diagnostic accuracy [10–12]. Specifically, models developed using MR data showed the potential of a universal model for cervical cancer identification and staging [13–15]. Applying a CNN to segment arteries in cervical PC MRI is challenging due to the number of arteries of interest (including right and left carotid and vertebral arteries) and the relatively low signal-to-noise ratio of the native images.

In this work, we present a CNN-based deep learning approach for segmenting carotid and vertebral arteries in PC MRI data from healthy control (HC) subjects and Moyamoya patients. Segmentations created by three different implementations were compared using the Dice Similarity Coefficient (DSC) for overlap and predicted bulk flow volume accuracy compared with manual segmentation.

2. Materials and Methods

2.1. Study Overview

The present study includes patient data from previously published work that assessed CBF using various MRI methods in HC subjects and Moyamoya patients enrolled from October 2015 to September 2021 [16]. All procedures were approved by the local Institutional Review Board of the institution of the senior author of this work (Ethics Committee Name: Research Compliance Office of Stanford University Approval Code: IRB Panel #5 Approval Date: 16 August 2023). The procedures were carried out according to the Declaration of Helsinki after participants had given written informed consent. In short, PC MRI data were collected using a simultaneous 3.0 T PET/MRI system (Signa, GE Healthcare, Waukesha, WI, USA) before and after the administration of acetazolamide (ACZ, or Diamox) at a dose of 15 mg/kg of the body weight with a maximum dose of 1000 mg [16]. The exclusion criteria for the patients were pregnancy, history of brain injury, impaired kidneys, and any contraindications to MRI or ACZ. Prior to the imaging sessions, all participants were instructed not to eat or drink anything containing caffeine at least 6 h before the study.

2.2. Study Population

As shown in the flow chart in Figure 1, a total of 176 HC subjects and Moyamoya patients were enrolled in this study. Among these participants, six of them withdrew from

the imaging session due to extenuating circumstances such as COVID-19, and 65 cases were excluded due to the poor quality of the PC MRI data assessed by a board-certified radiologist (GZ), resulting in 108 subjects that were scanned in pre- and post-Diamox conditions. A total of 107 HC subjects and 46 Moyamoya patients were included in this study.

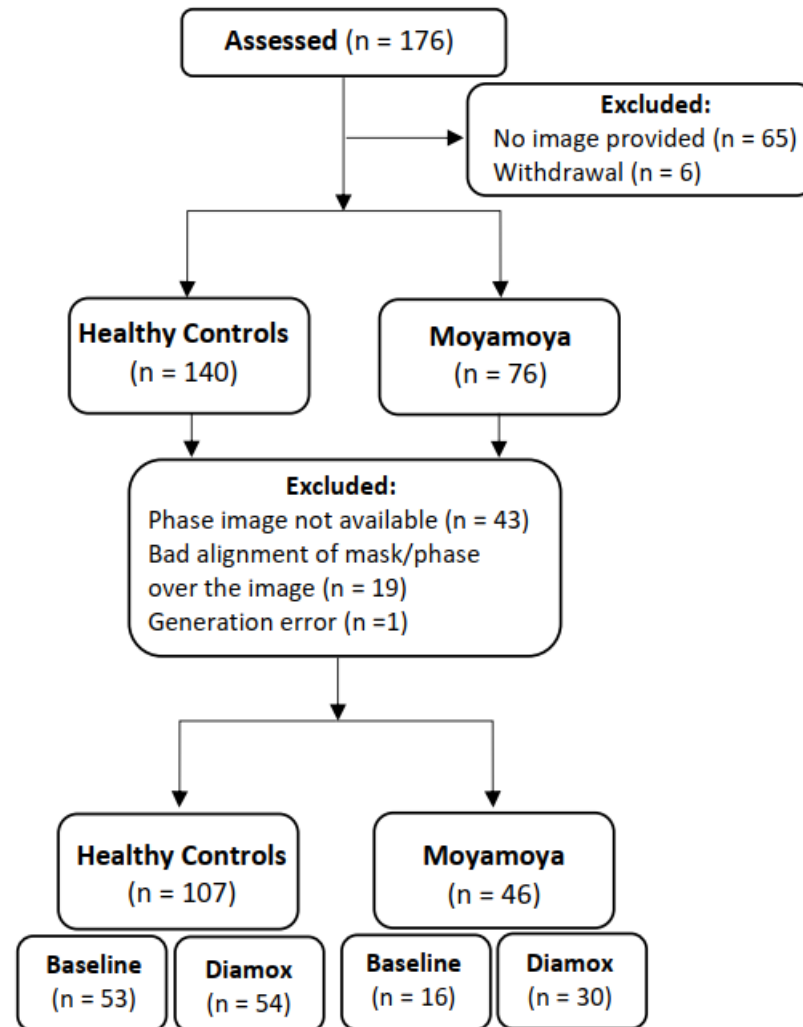


Figure 1. Flowchart showing the inclusion and exclusion criteria for this study. Overall, 153 subjects were enrolled; PC MRI data in 53 HC subjects and 16 Moyamoya patients were included in the baseline (pre-Diamox) condition; data in 54 HC subjects and 30 Moyamoya patients were included in the post-Diamox condition.

2.3. PC MRI Acquisition and Vessel Segmentation

PC MRI was performed using the scanning parameters in Table 1. The imaging slice was planned between C2 and C3 of the subject perpendicular to the vessels based on MR angiography. The magnitude and phase component (superior–inferior direction) of each PC MRI data were averaged across 10 cardiac phases retrospectively to create mean magnitude and phase images, which were used as the input for training the CNN network. As shown in Figure 2, the input data for the deep learning model was generated by concatenating the mean magnitude and phase components of the PC MRI data, resulting in a $2 \times 512 \times 512 \times 1$ tensor for each case.

Table 1. Scanning parameters for phase contrast MRI.

Parameters	Unit	Value
TR/TE	ms	12.4/4.6
Flip angle	degrees	20
FOV	mm	180 × 180
Matrix		512 × 512
Voxel size	mm	0.3516 × 0.3516 × 3
Cardiac phases		10
Average time per cardiac phase	ms	88
Slice thickness	mm	3
Number of slices		1
Velocity encoding	cm/s	100
Repeats		2
Scan duration	min	1:30

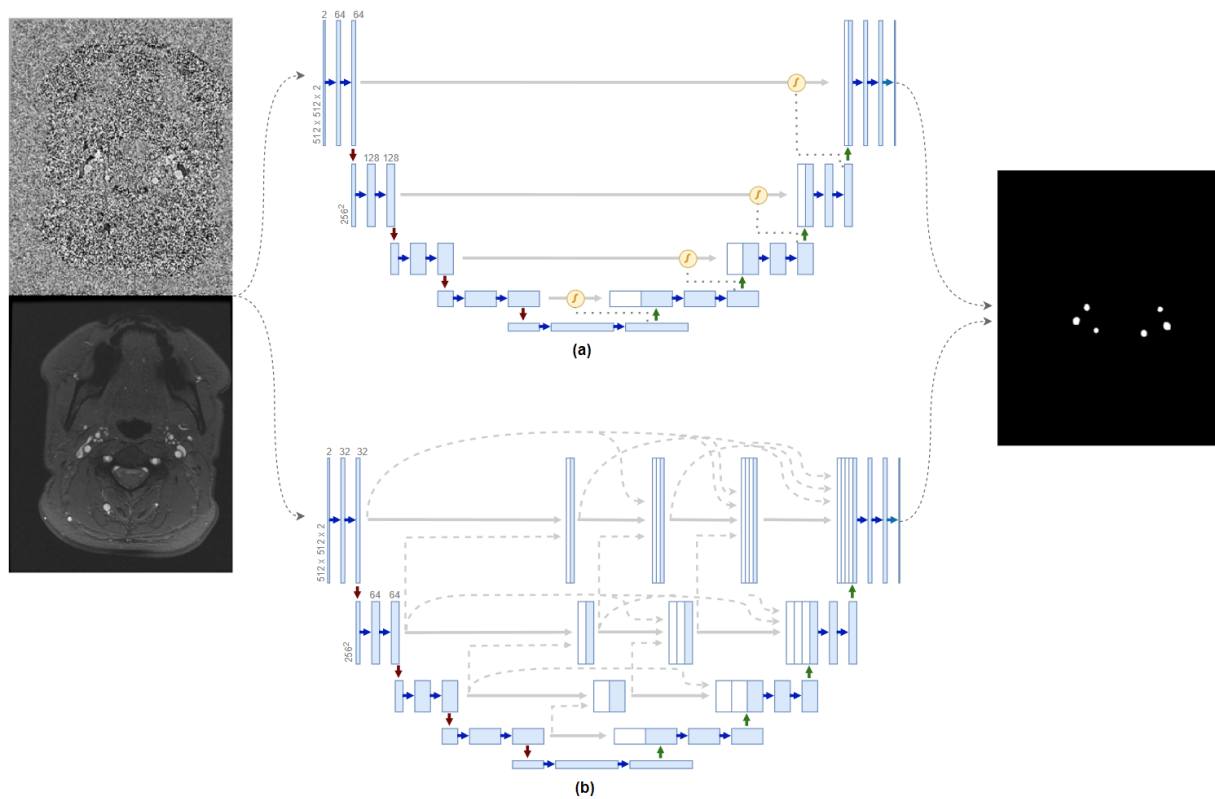


Figure 2. Deep learning network designs. (a) Attention U-Net and (b) Nested U-Net architecture. These two architectures differ on their approach to improved performance by using attention gates and extra skip-connections. U-Net without attention and nested structures were also used.

Using the mean magnitude images of the PC MRI data, six vessels of interest (right internal carotid artery [RICA], left internal carotid artery [LICA], right vertebral artery [RVA], left vertebral artery [LVA], right external carotid artery [RECA], left external carotid artery [LECA]) were segmented manually using the FSLeaves software version 6.0.7 (FSL, Oxford, UK). These segmented images were considered as the output (ground truth) for training the CNN network.

2.4. Mathematical Description of UNets

The U-Net model and other variants of it employ an encoder–decoder architecture at their core. This means they are mathematically divided into three types of 2D convolution functions: (1) downsampling/encoder functions e , whose domain is four times the size of their range, effectively halving a 2D image; (2) upsampling/decoder functions d , whose range is four times their domain, doubling the size of the image; and (3) transformation functions t , whose domain and range have the same dimension so they effectively only apply some transformation to the input image without changing its size.

All of the above functions are composed with a nonlinear function such as $\text{ReLU}(x) = \max(0, x)$ to allow stacking of complexity, since otherwise the stacked convolutions would be mathematically equivalent to a single convolution due to convolution being an associative operation.

A Standard U-Net consists of four encoder functions, four decoder functions, and $2k$ transformation functions, where k is the sum of kernel sizes for each depth, used to add more complexity between downsampling and upsampling. The differentiating idea is to connect the transformed output of the encoder and decoder functions that have the same range, effectively transferring spatial information (that is lost during subsequent downsampling) to decoder functions. These are called “skip connections”.

For Attention U-Net, the core idea is to add an “attention gating” mechanism that highlights certain parts of an image via depthwise multiplication with a weight matrix. This weight matrix is computed in the attention gate as follows:

$$\text{AttentionGate}(d_i, e_{i-1}) = \sigma(t(\text{ReLU}(t(d_i) + t(t_{e_{i-1}}(e_{i-1}))))))$$

Here, d_i and e_i are the output of the i th decoder function and encoder functions, respectively. d_{e_i} is a function that is the composition of transformations applied after encoder e_i . σ is the sigmoid function, which is applied elementwise. The output of the previously defined attention gate is a 2D matrix, which is depthwise multiplied with $t_{e_{i-1}}(e_{i-1})$, which is equivalent to the skip connection at depth $i - 1$.

For Nested U-Net (UNet++), the core idea is to extend the architecture of the U-Net by adding more transformation functions between skip connections and adding more skip connections in general. Since we have already laid the mathematical foundation of the constituents, their specific arrangement can be seen in Figure 2b.

2.5. Deep Learning Model Architecture, Training, and Testing

Three deep learning models were implemented and trained for the segmentation task: the original U-Net [17], an Attention U-Net [18], and a Nested U-Net [18]. As shown in Figure 2a, the attention U-Net is designed to focus on salient features of the image required for segmentation. As shown in Figure 2b, the Nested U-Net adds more skip pathways to reduce the semantic gap between the features of the encoder and decoder networks.

We divided the data into an 85–15% training validation split. Each model was trained for 1000 epochs on an RTX 3090 GPU. Adam was used as the optimizer for all models, and was initialized with a learning rate of 0.001 [19]. The learning rate was reduced by a factor of 2 every 30 epochs if the validation accuracy did not improve. Due to the small size of the training data, four data augmentation strategies were applied to facilitate model generalization of segmenting vessels while preventing overfitting:

1. $\pm 15^\circ$ rotation of the image;
2. ± 50 pixels image translation on the x and y axes;
3. 0.7 to 1.3 times image scaling;
4. $\pm 15^\circ$ image shear.

2.6. Flow Velocity and Volume Measurements

The phase images of the PC MRI data were used to quantify blood velocity. The area of each region of interest (ROI) was computed using the following equation:

$$ROI\ area = pixel\ area \times total\ pixel\ count$$

To account for the velocities measured in opposite directions, negative and positive velocities were averaged separately and summed to obtain the net average velocity. The volume flow was then computed using the following equation:

$$Net\ average\ volume\ flow = ROI\ area \times Net\ average\ velocity$$

3. Statistical Analysis

The receiver operating characteristic (ROC) curve was used to evaluate the performance of each model to segment the six arteries (left and right ICAs, ECAs, and VAs) on a pixel-by-pixel basis. False positives in this study included any segmentations made that were not part of the manual segmentation masks. The DSC, a metric that measures overlaps between two images, was calculated at the Youden index point of the deep learning model.

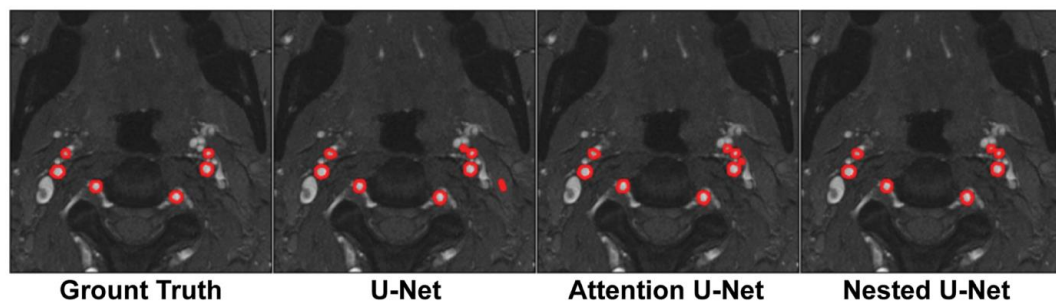
The segmentation results using the deep learning models were compared with the results obtained by manual segmentation (ground truth) using a Bland-Altman analysis. The Wilcoxon rank-sum tested average volume flows for each subset (HC and MM). Paired *t*-tests were conducted to compare the flow and volume measured by the deep learning models and the ground truth. The statistical significance level used for all tests was 0.05, and they were performed using MATLAB 2019a (MathWorks, Natick, MA, USA).

4. Results

4.1. Segmentation Results

Figure 3 shows the segmentation results from an HC subject and a patient with MM disease. In these example cases, all three deep learning models successfully segmented the six arteries of interest.

(A) Normal Subject



(B) Moyamoya Patient

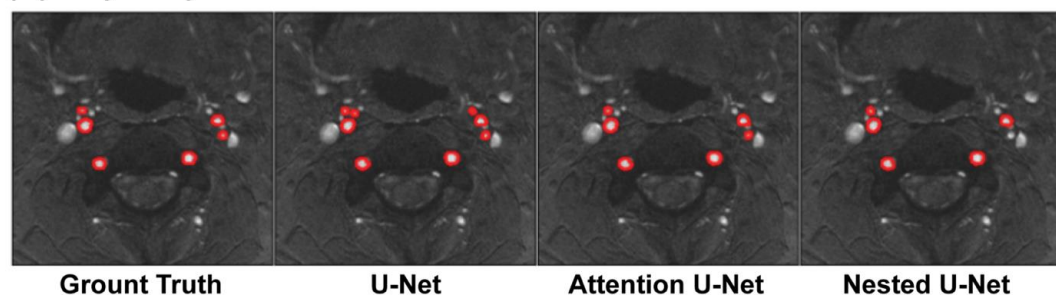


Figure 3. Segmentation results of the 3 deep learning models (U-Net, Attention U-Net, and Nested U-Net) in a HC subject and a Moyamoya patient. (A) Segmentation results in a normal subject.

(B) Segmentation results in a Moyamoya patient. Overall, all deep learning models successfully segmented the vessels of interest in pre-vasodilation conditions. The segmentation results in each model is shown in red circles.

Table 2 shows the DSC in both pre- and post-Diamox conditions for the three deep learning models. Figure 4 shows the ROC plot for all three models. The areas under the curves (AUCs) are likewise high for all models: 0.96, 0.99, and 0.98 for U-Net, Attention U-Net, and Nested U-Net, respectively. Nested U-Net outperformed the Attention U-Net when a decision threshold was chosen to minimize false positives; however, for all other decision thresholds, the Attention U-Net outperformed both other models.

Table 2. Dice scores achieved by each model using the manual segmentations as the ground truth.

	Healthy Control Baseline ($n = 53$)	Moyamoya Baseline ($n = 16$)	Healthy Control Diamox ($n = 54$)	Moyamoya Diamox ($n = 30$)	All Subjects in All Conditions ($n = 153$)
U-Net	0.92 ± 0.03	0.58 ± 0.31	0.92 ± 0.05	0.73 ± 0.18	0.81 ± 0.21
Attention U-Net	0.87 ± 0.06	0.69 ± 0.21	0.90 ± 0.05	0.76 ± 0.15	0.85 ± 0.13
Nested U-Net	0.85 ± 0.11	0.79 ± 0.21	0.91 ± 0.06	0.80 ± 0.13	0.85 ± 0.14

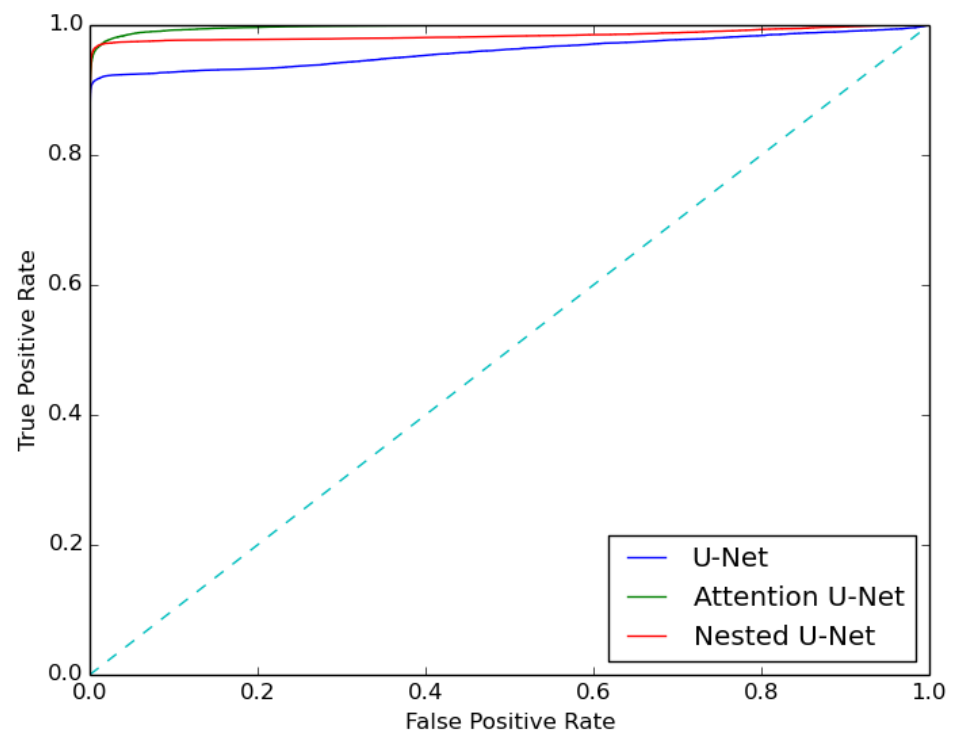


Figure 4. Receiver Operating Characteristic (ROC) curve for the Standard, Attention, and Nested U-Net Architectures. The areas under the curves (AUCs) are 0.96, 0.99, and 0.98 for U-Net, Attention U-Net, and Nester U-Net, respectively.

4.2. Flow and Velocity Measurements

Figure 5 shows the Bland-Altman analyses for the flow volume measured by the deep learning methods and ground truth. For both the HC and MM cohorts, good agreement in segmentation and flow volume measurements can be seen for all three deep learning models. The differences in flow between the ground truth and deep learning models ranged between ± 1.8 mL/s.

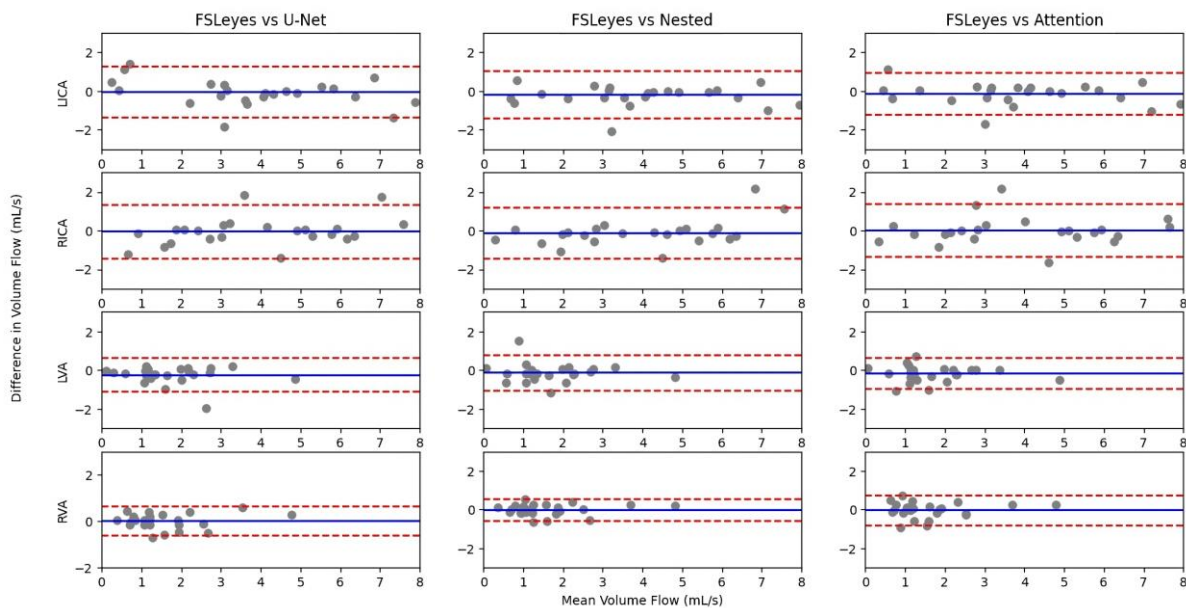


Figure 5. Bland–Altman plot comparing the flow volume measurements between the deep learning models and ground truth. Overall, good agreements were achieved for all 3 deep learning models. The blue line indicates the mean value and the red dash lines show the ± 1.96 SD.

5. Discussion

In this work, we demonstrated the effectiveness of applying deep learning models to segment arteries in PC MRI images and compute hemodynamic parameters. Specifically, we evaluated the effectiveness and accuracy of using both magnitude and phase parts of the PC MRI data as input for the deep learning model. The inclusion of phase contrast images gave the model the ability to measure flow velocity and volume within arteries of interest. Our data revealed that the model can efficiently segment the arteries of interests with low false positive rates and high DSC. Furthermore, all three models accurately estimated volume flow for healthy controls with Nested U-Net and Attention U-NET showing marginally higher accurate estimations than the Standard U-NET. The novelty and main contributions of this work include that (1) we utilized both magnitude and phase components of the MRI data for deep learning based segmentation tasks; and (2) our models were capable of detecting relatively small anatomical features in MRI data.

5.1. Performance of the Deep Learning Models

All three deep learning models performed well, with DSC higher than 0.80. Statistical results indicated that their similar dice scores achieved no significant difference in their detecting the arteries of interest. However, the Standard U-Net model showed lower accuracy in segmenting the vessels in Moyamoya patients than in the HC cohort, likely due to vessel occlusion and/or stenosis in Moyamoya cases. Interestingly, the Nested U-Net and Attention U-Net did not show this discrepancy while their performances were not significantly different from the Standard U-Net. These findings were further supported by the ROC curves of the three models, showing the Standard U-Net having generally lower AUC than the Attention and Nested U-Nets. It can also be observed that although the Attention U-Net can achieve better true positive performance than the Nested U-Net, the Nested U-Net marginally outperformed the Attention U-Net if minimizing false positives is desired. Based on these findings, Attention and Nested U-Nets should be the preferred choices due to their superior and non-discriminative performances over the Standard U-Net.

We avoided splitting the data into three sets due to the small size of our dataset. Instead, we employed a variety of augmentations to artificially reduce the dataset size to prevent overfitting, which left us with 20 samples for validation and 130 samples for

training. Dividing this data further into a test set would result in high variance estimates of test accuracy due to low sample count. The augmentations increased the number of images without increasing the underlying information content. In other words, all the augmentations of a given image would seem redundant to a human observer, since they would obviously depict the same underlying structure. However, these augmentations are non-trivial to our model and force invariance along certain axes that are obvious to humans such as rotations, translations, shears, etc. In total, a given image can appear in approximately at least 45 million different ways.

5.2. Flow Volume and Velocity Measurements

As expected by the model's performance based on DSC and ROC statistics, the models demonstrated similar performance for measuring flow volumes with the ground truth. Whilst Nested and Attention U-Nets were able to detect these arteries, the boundaries created for them may not be consistent with the ground truth, achieving a high DSC. The Bland-Altman analyses implied that when compared with the ground truth, the models achieved good agreement with most data points within the standard deviation limits. This was true for the Standard and Attention U-Net, showing potential for fine-tuned single artery accuracy for this application. Specifically, comparisons with the ground truth further exhibited that each artery had similar impacts of segmentation accuracy in the three deep learning models. In general, Nested U-Net showed the most promise among these three models in breaking the barrier between accurate segmentation results and flow calculation.

5.3. Comparison with Similar Studies on Image Segmentation

While image segmentation on phase contrast scans of the neck has not been broadly investigated in patients with cerebrovascular diseases, deep learning has been employed to perform similar tasks in lesion segmentation in patients with glioma or stroke. For instance, Kihira et al. applied the DenseNet121 based U-Net framework to identify and stage glioma using MR FLAIR data. A DSC score of 0.93 was achieved in a cohort consisting of 208 patients [20]. In terms of image segmentation for stroke patients, Shin et al. demonstrated that an efficient implementation of the Standard U-NET can achieve a DSC of 0.77 for segmenting stroke lesions in T1-weighted MRI scans [21].

The use of deep learning to segment objects of interest in MRI images is now a well-known approach. In this study, we focused on Standard U-Net and its variations, such as Attention and Nested (UNet++). However, in the field of medical imaging segmentation, there are several other state-of-the-art models used. For instance, the SegNet approach is an encoder–decoder network that produces class probabilities for each pixel. The encoder convolution produces feature maps using filter banks which are batch normalized and adjusted using $\text{ReLU} = \max(0, x)$. The 2×2 max-pooling and non-overlapping window results in the output being subsampled by a factor of 2. Each decoder corresponds to the 13 encoder layers and the final decoder output is sent to a soft-max classifier which independently classifies each pixel. Due to the use of pooling indices, the model works efficiently using low memory, but can be used for large images with high accuracy. While traditionally used for landscape segmentation, it was recently utilized successfully in medical imaging. Another study found that SegNet was better able to classify infected and non-infected lung tissue [22]. Its ability to segment landscapes was beneficial in distinguishing large features in normal and abnormal tissue. However, the loss of information during unpooling results in low resolution when compared to UNet models that use the entire feature map. The low resolution of this model would prevent it from providing accurate segmentation of small arteries and paired cerebral blood flow data. The ResUNet++ is an improvement based on the Deep Residual U-Net architecture, which combines U-Net and deep residual learning [23]. The ResUNet++ model utilizes the attention block, residual blocks, Atrous Spatial Pyramid Pooling (ASPP), and the squeeze and excitation block. The addition of deep residual learning decreases the reuse of features between blocks, therefore allowing

deeper neural networks that could resolve issues with degradation. The residual blocks combine the convolutional layers, batch normalization, and linear rectification (ReLU). Typically, there are three encoder layers with three corresponding decoder layers, as well as ASPP. The attention block helps generate more effective feature maps by analyzing which positions require more attention before the encoder units and ASPP allows for broader context after the encoder outputs are filtered. The output of the decoder is also fed to the ASPP, which results in a 1×1 convolution. The deep neural network of the model reduces percent error and allows higher image classification accuracy. ResUNet++ has been used to successfully segment lungs in chest X-ray images with a small data set and high accuracy, as well as distinguish different cardiovascular structures [24,25]. Compared to the UNet models used in our study, ResUNet++ has similar validation accuracy, but requires a much longer training time and more memory.

5.4. Implications of Results for General Readers

Our study focused on developing advanced artificial intelligence methods to identify important anatomical features in medical images. These methods were designed to improve clinical workflow whereby manual segmentation is needed to determine blood flow in arteries of the neck. The results from this study suggested that our methods successfully achieved these tasks in both normal subjects and patients in different physiological conditions. Our techniques presented in this work may be scaled and adapted to similar tasks of segmentation in medical imaging applications.

6. Limitations

The accuracy of the deep learning models was limited to select healthy control and Moyamoya cases when segmented by the Nested U-Net. Moyamoya patients have smaller arteries with generally lower blood flow, which may lead to relatively poorer segmentation accuracy. The arteries of interests in this study also are smaller 2D objects than the vessels typically used in cardiac studies previously used in DL studies [9]. This created a challenge for automatic segmentation, especially with the presence of other blood vessels of similar shape and even size. Other limitations included the requirements of having a reconstructed phase image based on several cardiac phases. The accuracy of our models was also limited by the small number of Moyamoya cases. Additional data augmentation may be considered to increase the number of training cases. Whilst we understand that there are various other implementations of the standard U-NET for image segmentation tasks and the importance of comparison between these techniques, we presented two such implementations and their results in this work. Since our institution treats several new Moyamoya patients each month, we will consider adopting different U-Net structures, such as UNet++ and MAnet, in future studies. Furthermore, the performance of the model may also be improved by including additional MR scans (such as MRA) obtained in the same session. Other challenges regarding data leaking may also need more systematic investigation to improve the performance of the segmentation algorithm.

7. Conclusions

This study demonstrated the effectiveness of deep learning to segment cervical arteries on PC MR scans, allowing the quantification of flow volume.

Author Contributions: Methodology, B.C., D.Y., R.H., M.Y.Z. and G.Z.; Investigation, E.T.; Resources, K.H., D.H., M.K. and G.A.D.; Writing—original draft, B.C., D.Y. and M.Y.Z.; Writing—review & editing, G.Z.; Supervision, G.K.S., M.M., M.Y.Z. and G.Z.; Project administration, S.H.; Funding acquisition, M.J., M.Y.Z. and G.Z. All authors have read and agreed to the published version of the manuscript.

Funding: This work is supported by the American Heart Association (Grant: 826254), National Institutes of Health (Grants: R01EB025220-02, P30AG066515, and 4R00NS102884-03), and Research Experience for Undergraduates (REU) Program at Department of Radiology Stanford School of Medicine.

Institutional Review Board Statement: The study was conducted in accordance with the Declaration of Helsinki, and approved by the Institutional Review Board of Stanford University (protocol code 31766, 25 August 2015).

Informed Consent Statement: Informed consent was obtained from all subjects involved in the study.

Data Availability Statement: The data presented in this study are available on request from the corresponding author.

Conflicts of Interest: The authors declared the following potential conflicts of interest with respect to the research, authorship, and/or publication of this article: Greg Zaharchuk received funding support through GE Healthcare and Bayer Healthcare and equity from Subtle Medical. Gary K Steinberg is a consultant for Peter Lasic US, NeuroSave, SanBio, Zeiss, and Surgical Theater.

Abbreviations

ACZ	acetazolamide
AUC	area under the curve
CBF	cerebral blood flow
CNN	convolutional neural network
DSC	Dice similarity coefficient
HC	healthy control
LECA	left external carotid artery
LICA	left internal carotid artery
LVA	left vertebral artery
MM	moyamoya
MRI	magnetic resonance imaging
PC	phase contrast
RECA	right external carotid artery
RICA	right internal carotid artery
ROI	region of interest
ROC	receiver operating characteristic
RVA	right vertebral artery

References

- De Boorder, M.J.; Hendrikse, J.; van der Grond, J. Phase-Contrast Magnetic Resonance Imaging Measurements of Cerebral Autoregulation with a Breath-Hold Challenge: A Feasibility Study. *Stroke* **2004**, *35*, 1350–1354. [[CrossRef](#)] [[PubMed](#)]
- Steinberg, G.K.; Gooderham, P.A. Intracranial-Extracranial Bypass Surgery for Moyamoya Disease. In *Neurovascular Surgery*; Kalani, Y., Nakaji, P., Spetzler, R.F., Eds.; Thieme: New York, NY, USA, 2015; ISBN 978-1-60406-760-6.
- Lee, M.; Zaharchuk, G.; Guzman, R.; Achrol, A.; Bell-Stephens, T.; Steinberg, G.K. Quantitative Hemodynamic Studies in Moyamoya Disease: A Review. *Neurosurg. Focus* **2009**, *26*, E5. [[CrossRef](#)] [[PubMed](#)]
- Liu, P.; Qi, Y.; Lin, Z.; Guo, Q.; Wang, X.; Lu, H. Assessment of Cerebral Blood Flow in Neonates and Infants: A Phase-Contrast MRI Study. *NeuroImage* **2019**, *185*, 926–933. [[CrossRef](#)] [[PubMed](#)]
- Alperin, N.; Vikingstad, E.M.; Gomez-Anson, B.; Levin, D.N. Hemodynamically Independent Analysis of Cerebrospinal Fluid and Brain Motion Observed with Dynamic Phase Contrast MRI. *Magn. Reson. Med.* **1996**, *35*, 741–754. [[CrossRef](#)] [[PubMed](#)]
- Khan, M.A.; Liu, J.; Tarumi, T.; Lawley, J.S.; Liu, P.; Zhu, D.C.; Lu, H.; Zhang, R. Measurement of Cerebral Blood Flow Using Phase Contrast Magnetic Resonance Imaging and Duplex Ultrasonography. *J. Cereb. Blood Flow Metab.* **2017**, *37*, 541–549. [[CrossRef](#)] [[PubMed](#)]
- Zhou, S.K.; Greenspan, H.; Davatzikos, C.; Duncan, J.S.; Van Ginneken, B.; Madabhushi, A.; Prince, J.L.; Rueckert, D.; Summers, R.M. A Review of Deep Learning in Medical Imaging: Imaging Traits, Technology Trends, Case Studies with Progress Highlights, and Future Promises. *Proc. IEEE* **2021**, *109*, 820–838. [[CrossRef](#)] [[PubMed](#)]
- Salem, M.; Valverde, S.; Cabezas, M.; Pareto, D.; Oliver, A.; Salvi, J.; Rovira, À.; Lladó, X. A fully convolutional neural network for new T2-w lesion detection in multiple sclerosis. *NeuroImage Clin.* **2020**, *25*, 102149. [[CrossRef](#)] [[PubMed](#)]
- Bratt, A.; Kim, J.; Pollie, M.; Beecy, A.N.; Tehrani, N.H.; Codella, N.; Perez-Johnston, R.; Palumbo, M.C.; Alakbarli, J.; Colizza, W.; et al. Machine Learning Derived Segmentation of Phase Velocity Encoded Cardiovascular Magnetic Resonance for Fully Automated Aortic Flow Quantification. *J. Cardiovasc. Magn. Reson.* **2019**, *21*, 1. [[CrossRef](#)]
- Pacal, I.; Kılıcarslan, S. Deep Learning-Based Approaches for Robust Classification of Cervical Cancer. *Neural Comput. Appl.* **2023**, *35*, 18813–18828. [[CrossRef](#)]
- Attallah, O. Cervical Cancer Diagnosis Based on Multi-Domain Features Using Deep Learning Enhanced by Handcrafted Descriptors. *Appl. Sci.* **2023**, *13*, 1916. [[CrossRef](#)]

12. Chen, C.; Cao, Y.; Li, W.; Liu, Z.; Liu, P.; Tian, X.; Sun, C.; Wang, W.; Gao, H.; Kang, S.; et al. The Pathological Risk Score: A New Deep Learning-Based Signature for Predicting Survival in Cervical Cancer. *Cancer Med.* **2023**, *12*, 1051–1063. [[CrossRef](#)] [[PubMed](#)]
13. Lin, Y.-C.; Lin, Y.; Huang, Y.-L.; Ho, C.-Y.; Chiang, H.-J.; Lu, H.-Y.; Wang, C.-C.; Wang, J.-J.; Ng, S.-H.; Lai, C.-H.; et al. Generalizable Transfer Learning of Automated Tumor Segmentation from Cervical Cancers toward a Universal Model for Uterine Malignancies in Diffusion-Weighted MRI. *Insights Imaging* **2023**, *14*, 14. [[CrossRef](#)] [[PubMed](#)]
14. Zaki, N.; Qin, W.; Krishnan, A. Graph-Based Methods for Cervical Cancer Segmentation: Advancements, Limitations, and Future Directions. *AI Open* **2023**, *4*, 42–55. [[CrossRef](#)]
15. Jin, S.; Xu, H.; Dong, Y.; Hao, X.; Qin, F.; Xu, Q.; Zhu, Y.; Cong, F. Automatic Cervical Cancer Segmentation in Multimodal Magnetic Resonance Imaging Using an EfficientNet Encoder in UNet++ Architecture. *Int. J. Imaging Syst. Technol.* **2023**, *33*, 362–377. [[CrossRef](#)]
16. Zhao, M.Y.; Fan, A.P.; Chen, D.Y.-T.; Sokolska, M.J.; Guo, J.; Ishii, Y.; Shin, D.D.; Khalighi, M.M.; Holley, D.; Halbert, K.; et al. Cerebrovascular Reactivity Measurements Using Simultaneous 15O-Water PET and ASL MRI: Impacts of Arterial Transit Time, Labeling Efficiency, and Hematocrit. *NeuroImage* **2021**, *233*, 117955. [[CrossRef](#)] [[PubMed](#)]
17. Ronneberger, O.; Fischer, P.; Brox, T. U-Net: Convolutional Networks for Biomedical Image Segmentation. *arXiv* **2015**, arXiv:1505.04597.
18. Zhou, Z.; Siddiquee, M.M.R.; Tajbakhsh, N.; Liang, J. UNet++: A Nested U-Net Architecture for Medical Image Segmentation. *arXiv* **2018**, arXiv:1807.10165.
19. Kingma, D.P.; Ba, J. Adam: A Method for Stochastic Optimization. *arXiv* **2017**, arXiv:1412.6980.
20. Kihira, S.; Mei, X.; Mahmoudi, K.; Liu, Z.; Dogra, S.; Belani, P.; Tsankova, N.; Hormigo, A.; Fayad, Z.A.; Doshi, A.; et al. U-Net Based Segmentation and Characterization of Gliomas. *Cancers* **2022**, *14*, 4457. [[CrossRef](#)]
21. Shin, H.; Agyeman, R.; Rafiq, M.; Chang, M.C.; Choi, G.S. Automated Segmentation of Chronic Stroke Lesion Using Efficient U-Net Architecture. *Biocybern. Biomed. Eng.* **2022**, *42*, 285–294. [[CrossRef](#)]
22. Saood, A.; Hatem, I. COVID-19 Lung CT Image Segmentation Using Deep Learning Methods: U-Net versus SegNet. *BMC Med. Imaging* **2021**, *21*, 19. [[CrossRef](#)]
23. Jha, D.; Smedsrud, P.H.; Riegler, M.A.; Johansen, D.; de Lange, T.; Halvorsen, P.; Johansen, H.D. ResUNet++: An Advanced Architecture for Medical Image Segmentation. In Proceedings of the 2019 IEEE International Symposium on Multimedia (ISM), San Diego, CA, USA, 9–11 December 2019.
24. Ibrahim, S.; Elgohary, K.; Higazy, M.; Mohannad, T.; Selim, S.; Elattar, M. Lung Segmentation Using ResUnet++ Powered by Variational Auto Encoder-Based Enhancement in Chest X-Ray Images. In *Medical Image Understanding and Analysis, Proceedings of the 26th Annual Conference, MIUA 2022, Cambridge, UK, 27–29 July 2022*; Yang, G., Aviles-Rivero, A., Roberts, M., Schönlieb, C.-B., Eds.; Springer International Publishing: Cham, Switzerland, 2022; pp. 339–356.
25. Habijan, M.; Galić, I.; Romić, K.; Leventić, H. AB-ResUNet+: Improving Multiple Cardiovascular Structure Segmentation from Computed Tomography Angiography Images. *Appl. Sci.* **2022**, *12*, 3024. [[CrossRef](#)]

Disclaimer/Publisher’s Note: The statements, opinions and data contained in all publications are solely those of the individual author(s) and contributor(s) and not of MDPI and/or the editor(s). MDPI and/or the editor(s) disclaim responsibility for any injury to people or property resulting from any ideas, methods, instructions or products referred to in the content.